Supporting Information

Template-free synthesis of single-crystal SrTiO$_3$ nanocages for photocatalytic overall water splitting

Jian Zhang[a†], Yang Zhang[a†], Yu Peng[a], Meng Min Wang[a], Yan Zhu[a], Xing Wang[a], Yu Yang Tang[a], Peng Cheng Ding[a], Peng Fei Liu[a*] and Hua Gui Yang[a*]

[a] Key Laboratory for Ultrafine Materials of Ministry of Education, School of Materials Science and Engineering, East China University of Science and Technology, Shanghai 200237, China

† These authors contributed equally to this work.

* Corresponding Authors: Email: pfliu@ecust.edu.cn (Peng Fei Liu), hgyang@ecust.edu.cn (Hua Gui Yang)

Experimental Section

Materials.

Titanium chloride solution (15.0~20.0 % $TiCl_3$ in 30 % HCl, AR) was purchased from Aladdin. Strontium chloride hexahydrate ($SrCl_2 \cdot 6H_2O$, 99.99%) and ethanol (EtOH, AR) were bought from Sinopharm Chemical Reagent. Lithium hydroxide monohydrate ($LiOH \cdot H_2O$, 98%) and ethylene glycol were received from Alfa Aesar.

All the chemicals were used as received without any further purification. Ultrapure water (Millipore Milli-Q grade) with a resistivity of 18.2 MΩ cm at 25 °C was used throughout all the experiments.

Synthesis of SrTiO$_3$ (STO) nanosphere precursor.

The nanosphere STO precursor was synthesized through a modified hydrothermal reaction, according to a previously reported method. Typically, 0.8 mL of $TiCl_3$ solution was added into 25 mL ultrapure water containing 0.9 mL ethylene glycol cooled in an ice bath and stirred for 5 min. 30 mL of LiOH solution containing 4.0 g $LiOH \cdot H_2O$ was then added. After stirring for 15 min, 0.74 g $SrCl_2 \cdot 6H_2O$ was added and stirred for additional 7 min. Subsequently, the mixed feedstock was transferred to a 100 mL Teflon-lined stainless-steel autoclave and reacted at 180 °C for 2~4 h. After reaction, the autoclave was submerged directly in ice water for rapid cooling and the precipitate was recovered by centrifugation, washed with ultrapure water and ethanol until no precipitation in the separated supernatant when the $AgNO_3$ solution was added and then dried at 60 °C in vacuum drying chamber.

Synthesis of porous SrTiO$_3$ (P-STO).

The hydrothermal reaction procedure is consistent with that of nanosphere STO precursor, and the reaction was maintained at 180 °C for 48 h. After the reaction, the autoclave was cooled naturally and the precipitate was recovered by centrifugation, washed with ultrapure water and ethanol until no precipitation in the separated supernatant when the $AgNO_3$ solution was added and then dried at 60 °C in vacuum drying chamber.

Synthesis of nanocage-shaped SrTiO₃ single crystals (N-STO).

N-STO was synthesized in a $SrCl_2 \cdot 6H_2O$ molten salt. In a typical synthesis, the prepared nanosphere STO precursor was mixed with $SrCl_2 \cdot 6H_2O$ in a 1:10 molar ratio. This mixture was then heated in a muffle furnace at a rate of 5 °C/min to a temperature range of 800 °C to 820 °C. Upon reaching the target temperature, the mixture was rapidly quenched by immediate removal from the muffle furnace. After cooling to room temperature, the product was separated from excess $SrCl_2$ by centrifugal washes with ultrapure water for three times and then dried at 60 °C in vacuum drying chamber.

Characterization of materials.

The crystal structure of as-prepared samples was determined by X-ray diffraction (XRD) from Bruker D8 Advanced Diffractometer with Cu Kα radiation (λ = 1.5406 Å) at the scanning speed of 4 °/min. The morphology was examined by field emission scanning electron microscope (FE-SEM, HITACHI S4800). High-resolution transmission electron microscopy (HRTEM) characterization was performed using ThermoFisher Talos F200X (FETEM, 200 kV). Raman spectra were recorded on a Renishaw in Via Raman microscope in the range of 100–1200 cm^{-1} under a 514 nm laser excitation. FT-IR spectra were measured using KBr pellets on a INVENIO (Bruker) FT-IR spectrometer in the range of 4000−400 cm^{-1}.The light absorption range of the photocatalysts were carried out by ultraviolet-visible (UV-vis) spectrophotometry with a UV-vis spectrophotometer (CARY 500). X-ray photoelectron spectroscopy (XPS) was performed on ESCALAB 250 Xi X-ray photoelectron spectrometer using a monochromatized Al Kα X-ray source (hv = 1486.6 eV) to investigate surface elements content and valence of as-prepared samples. The XPS data were calibrated by the binding energy of C 1s peak at 284.8 eV. X-band electron paramagnetic resonance (EPR) spectra was performed with a Bruker ER200D instrument at 9.86 GHz and 20 mW to analyze electronic structural changes. Ultraviolet photoelectron spectroscopy (UPS, PHI 5000 Versaprobe II) was conducted to determine the VBM of semiconductors using He I (21.22 eV) as the excitation source at an applied bias voltage of 10 eV. Photoluminescence (PL) spectra was obtained on an FLS1000 spectrofluorometer (Edinburgh Instruments) at room temperature. Time-resolved photoluminescence (TR-PL)

spectra was conducted on Hitachi FL4700 to investigate the precise life time of electron-hole pairs. Samples were tested for nitrogen adsorption-desorption using Micromeritics® TriStar II Plus.

Photoelectrode preparation and photoelectrochemical performance measurements.

The working electrode was fabricated using fluorine-doped tin oxide (FTO) glass substrates. The FTO glass was subjected to sequential sonication in soap water, deionized water, acetone, and ethanol to ensure cleanliness. Subsequently, 3 mg of the photocatalyst was dispersed in a solution comprising 1 mL of isopropanol and 20 µL of Nafion solution, and the mixture was sonicated to form a homogeneous suspension. This suspension was then uniformly sprayed onto the conductive surface of the FTO glass, forming a photocatalyst film with an active area approximating 1×1 cm². The resulting working electrodes were dried thoroughly and reserved for subsequent experimental use.

The photoelectrochemical performance assessments were conducted within a conventional three-electrode electrochemical cell. The sample served as the working electrode, while a platinum (Pt) plate and an Ag/AgCl electrode functioned as the counter and reference electrodes, respectively. The electrodes were immersed in a 0.5 M Na_2SO_4 electrolyte solution. Illumination was provided by a 300W xenon lamp ($\lambda > 300$ nm, Perfectlight Sci & Tech, PLS-SXE-300+). Mott-Schottky characterization was performed at Autolab Vionic electrochemical workstation with test frequencies set to 1000, 1500, and 2000 Hz.

Photocatalytic activities measurements.

The photocatalytic water splitting reactions were carried out in a Pyrex top-irradiation reaction vessel connected to a glass gas-closed-circulation system (Perfectlight Sci & Tech, Labsolar 6A) with a top irradiation-type reaction vessel. The reaction solution was evacuated several times to remove air completely prior to irradiation under a 300W xenon lamp (>300nm, Perfectlight Sci & Tech, PLS-SXE-300+). The temperature of the reaction solution was maintained at 298K by the flow of cooling water during the reaction. The evolved gases were

analyzed by gas chromatography (Fuli, GC-9790-II), with a thermal conductive detector and 5Å molecular sieve column, using Ar as the carrier gas.

Before to the photocatalytic test, aqueous solutions of $RhCl_3 \cdot 6H_2O$, K_2CrO_4 and $Co(NO_3)_2 \cdot 6H_2O$ were prepared. The concentration of the metal species (Rh, Cr and Co) was 2 mg mL^{-1}. As a precursor solution for subsequent photodeposition cocatalysts.

In the photocatalytic hydrogen evolution half-reaction, 25 mg of the photocatalyst was dispersed in 50 mL of deionized water containing 10 vol% triethanolamine as a sacrificial agent. To deposit 0.4 wt% Rh and 0.2 wt% Cr on 25 mg of N-STO or P-STO, the $RhCl_3 \cdot 6H_2O$ aqueous solution (50 μL) was first added to the reaction suspension with magnetic stirring, and the resulting suspension was irradiated with a Xe lamp (300 W, full arc) for 10 minutes to facilitate the cocatalyst (Rh) loading. Following this, the K_2CrO_4 aqueous solution (25 μL) was introduced, and the suspension was irradiated for an additional 5 minutes to facilitate the cocatalyst (Cr_2O_3) loading. The evolved hydrogen gas was periodically quantified under continuous illumination.

In the photocatalytic oxygen evolution half-reaction, 25 mg of photocatalyst was dispersed in 50 mL of 0.02 mM $AgNO_3$ solution and 50 mg of La_2O_3 was added as a pH modifier. To deposit 0.4 wt% Co on 25 mg of N-STO or P-STO, the $Co(NO_3)_2 \cdot 6H_2O$ aqueous solution (50 μL) was added to the reaction suspension under magnetic stirring, and then the resulting suspension was irradiated with an Xe lamp (300 W, full arc) for 5 min to facilitate the cocatalyst (CoOOH) loading. The evolved oxygen gas was periodically quantified under continuous illumination.

In a standard photocatalytic overall water splitting experiment, 25 mg of the photocatalyst was dispersed in 50 mL of deionized water. To deposit 0.4 wt% Rh, 0.2 wt% Cr and 0.2 wt% Co on 25 mg of N-STO or P-STO, the $RhCl_3 \cdot 6H_2O$ aqueous solution (50 μL) was first added to the reaction suspension with magnetic stirring, and the resulting suspension was irradiated with a Xe lamp (300 W, full arc) for 30 minutes to facilitate the cocatalyst (Rh) loading. Subsequently, the K_2CrO_4 aqueous solution (25 μL) was introduced, and the suspension was irradiated for an additional 15 minutes to facilitate the cocatalyst (Cr_2O_3) loading. Following this, the $Co(NO_3)_2 \cdot 6H_2O$ aqueous solution (25 μL) was incorporated, and the suspension was irradiated

for an additional 15 minutes to facilitate the cocatalyst (CoOOH) loading. The evolution of gaseous products was monitored at regular intervals under continuous illumination.

Apparent quantum yield measurements.

The H_2 evolution rate was measured in the photocatalytic overall water splitting experiment. To determine the wavelength dependence of the AQY, samples were irradiated with monochromatic light generated by an Xe lamp and sent through bandpass filters with central wavelengths of 280 nm, 313 nm, 334 nm, 350 nm, 360 or 370 nm (Optics). The full-width at half-maximum of each of these bandpass filters was approximately 10 nm.

The AQY was calculated according to the following equation:

$$AQY = \frac{Number\ of\ reacted\ electrons}{Number\ of\ incident\ photons} \times 100\% = \frac{2 \times n \times N_A}{S \times P \times t \times \dfrac{\lambda}{h \times c}} \times 100$$

where n is the amount of H_2 molecules (μmol) per hour; N_A is the Avogadro constant (6.022×10^{23} mol^{-1}); S is the irradiation area (cm^2); P is the monochromatic light intensity (mW/cm^2); t is the light irradiation time (s); λ is the wavelength of the monochromatic light (nm); h is the Plank constant (6.626×10^{-34} J s); c is the speed of light (3×10^8 m·s^{-1}).

Taking monochromatic light at 280nm measurement (Tab. S1) as an example, AQY was calculated as follows:

$$AQY = \frac{Number\ of\ reacted\ electrons}{Number\ of\ incident\ photons} \times 100\% = \frac{2 \times n \times N_A}{S \times P \times t \times \dfrac{\lambda}{h \times c}} \times 100\%$$

$$= \frac{2 \times 0.3 \times 10^{-6} \times 6.022 \times 10^{23}}{19.6 \times 3.76 \times 10^{-3} \times 3600 \times \dfrac{280 \times 10^{-9}}{6.626 \times 10^{-34} \times 3 \times 10^8}} \times 100\%$$

$$= 0.967\ \text{‰}$$

Supplementary Figures and Tables
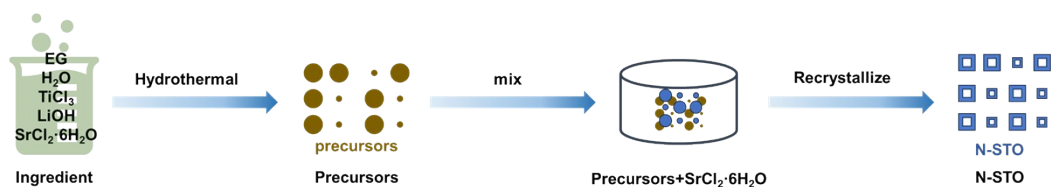
Fig. S1 Schematic representation of the synthesis route for N-STO. First, the spherical precursor was prepared by a hydrothermal method, then mixed with $SrCl_2 \cdot 6H_2O$ and then recrystallized by high-temperature solid-phase recrystallization to nanocage-shaped $SrTiO_3$.
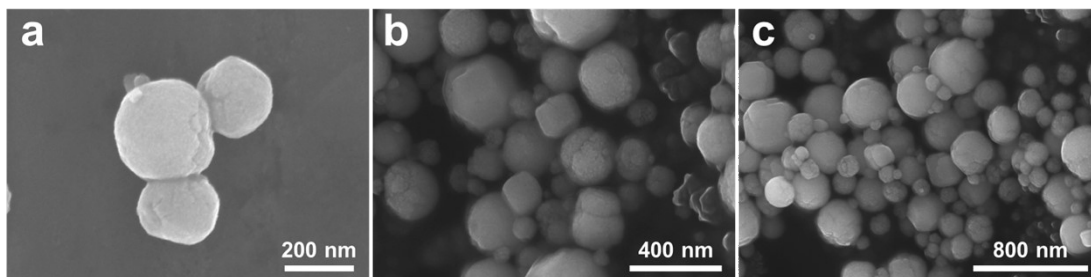
Fig. S2 (a-c) SEM images of spherical STO precursors, showing the spherical morphology with rough surface of precursor.
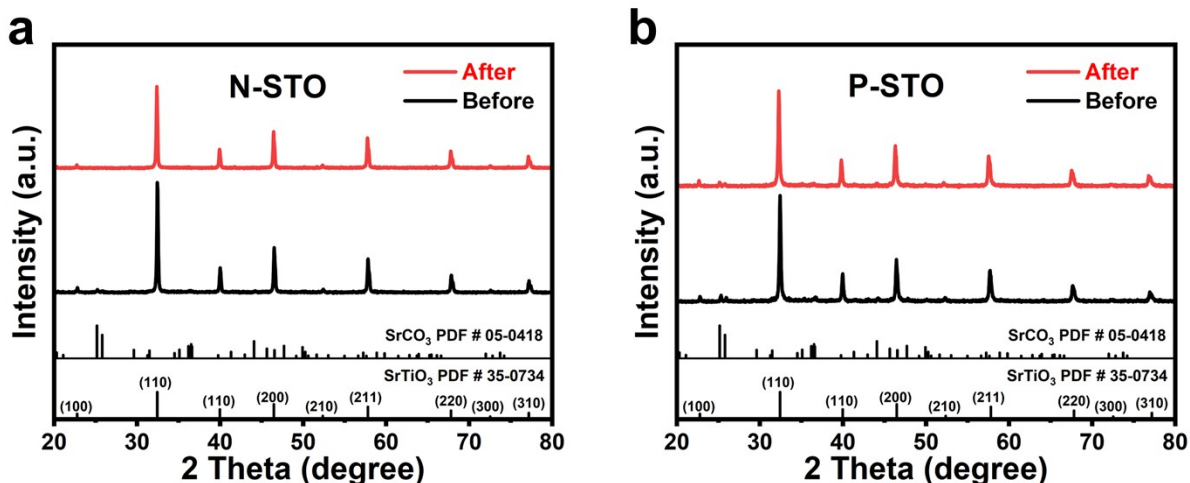
Fig. S3 (a, b) Comparison of the XRD spectra of P-STO and N-STO before the photocatalytic reaction and after the photocatalytic overall water splitting reaction for 3 hours, respectively. The figure shows that the P-STO and N-STO samples before photocatalytic testing have $SrCO_3$ phases. However, in the XRD patterns of the post-photocatalytic samples, no distinct diffraction peaks assigned to $SrCO_3$ were observed notably, while prominent peaks associated with STO remain. Although a weak peak of the $SrCO_3$ phase is still present in P-STO, this is due to the greater amount of $SrCO_3$ in P-STO compared to that in N-STO. This indicates that $SrCO_3$ impurities are not embedded in the crystal bulk and would undergo decomposition during the photocatalytic reaction. After 3 hours of reaction, $SrCO_3$ was no longer detectable, and Figure 4d shows that the photocatalytic activity remains stable over 25 hours. This indicates that the decomposition of $SrCO_3$ does not negatively impact the photocatalytic performance of $SrTiO_3$.
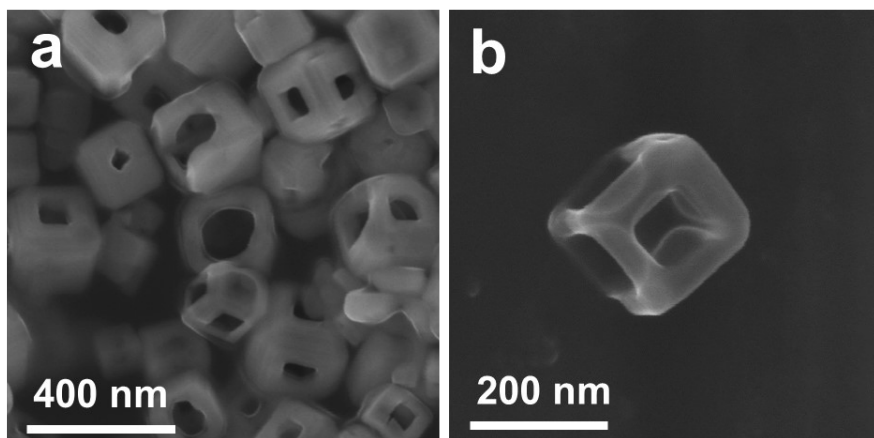
Fig. S4 (a, b) SEM images of N-STO, exhibiting nano-cage morphology.
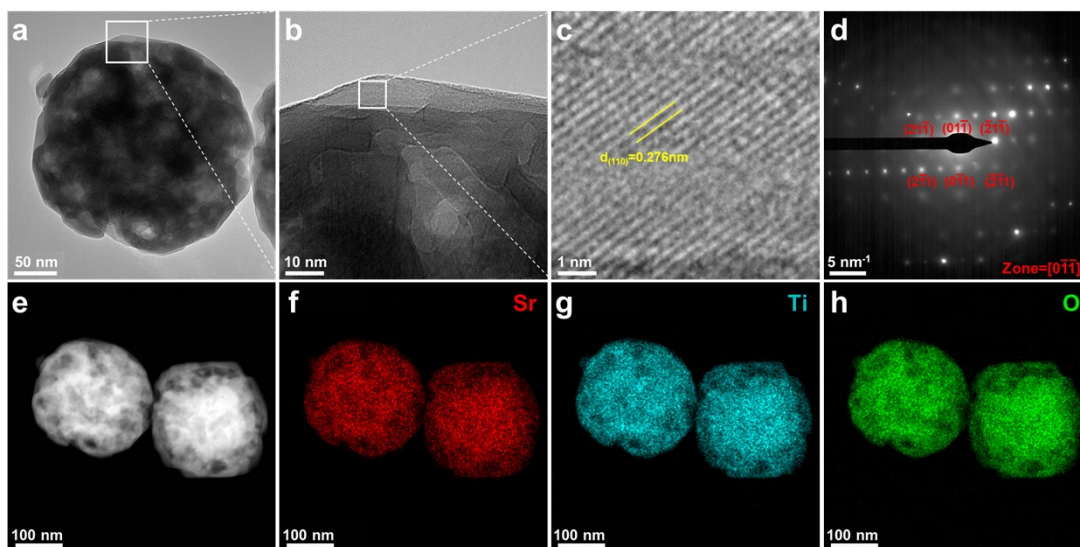
Fig. S5 (a) TEM image, (b, c) HRTEM images and (d) SAED pattern of P-STO. (e) HAADF image and (f-h) corresponding elemental maps of Sr, Ti, and O, respectively, demonstrating the porous nature of P-STO.
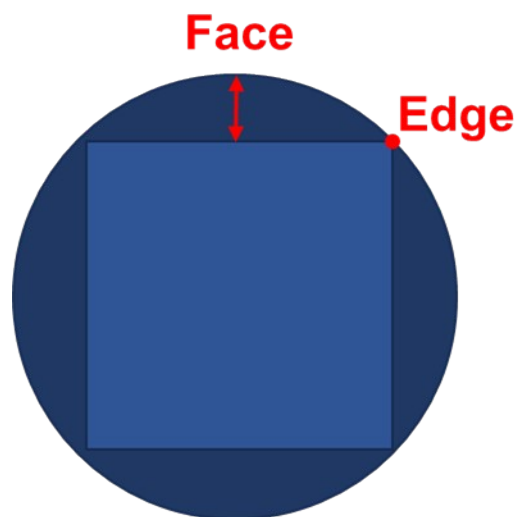
Fig. S6 Hypothetical crystal transformation process of the STO precursor from spherical to cubic morphology, illustrating that the faces of the cubic structure are distanced further from their corresponding spherical surfaces, while the edges of the cubic structure are in closer proximity to the corresponding spherical surfaces.
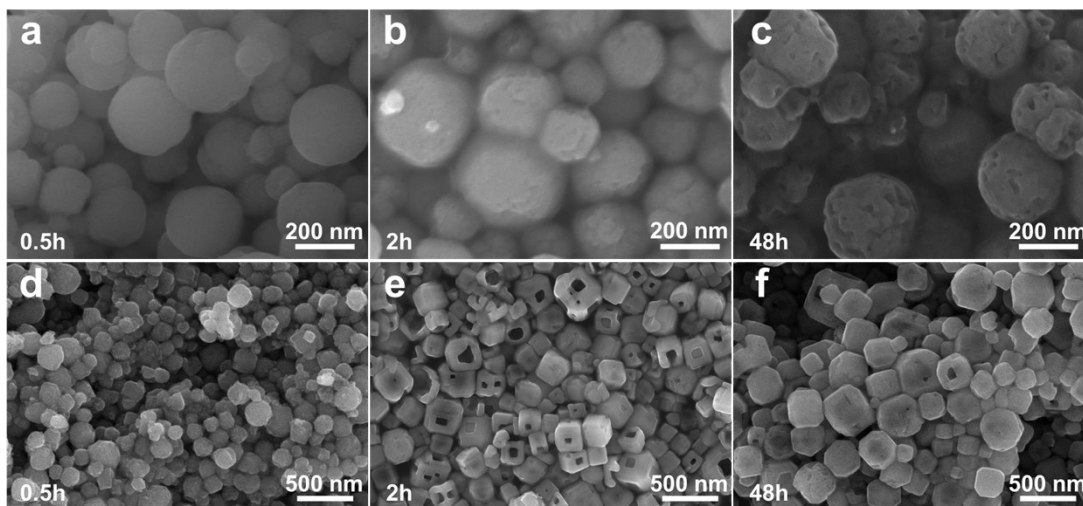
Fig. S7 (a-c) SEM images of STO precursor treated hydrothermally for 0.5 h, 2 h, and 48 h. (d-f) SEM images corresponding to the STO precursor after heating at 820°C using the molten salt method. The hydrothermal 0.5h and 48h precursors did not exhibit nanocage structures after heating, and only the hydrothermal 2h precursor exhibited a unique nanocage-shaped structure after heating.
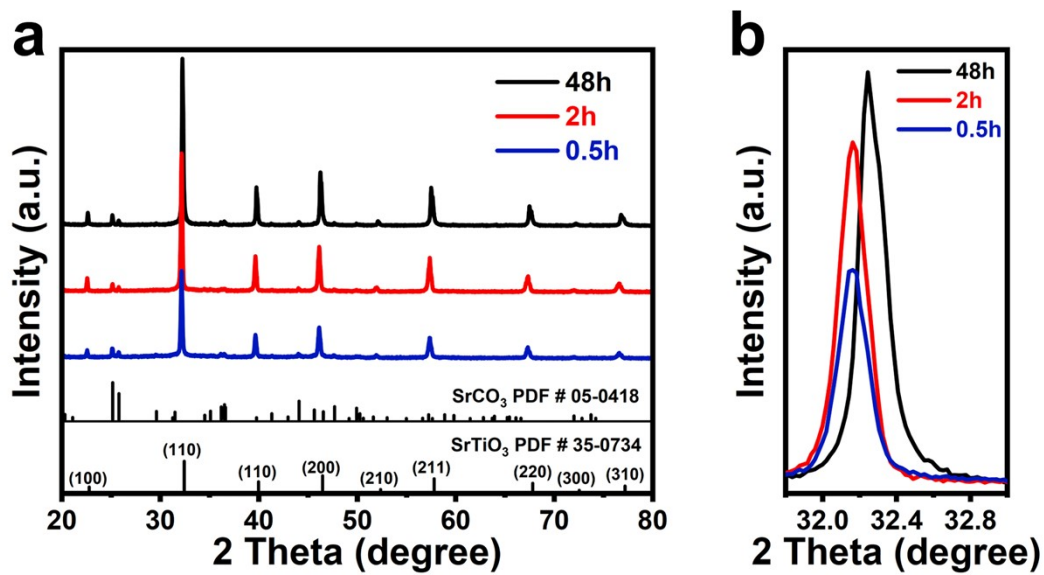
Fig. S8 (a) XRD patterns of STO precursor treated hydrothermally for 0.5 h, 2 h, and 48 h. (b) Comparative analysis of the main peak at 32.4° among the samples, demonstrating that the precursor with 48h of hydrothermal heating had the highest crystallinity, followed by 2h, and 0.5h had the lowest crystallinity.
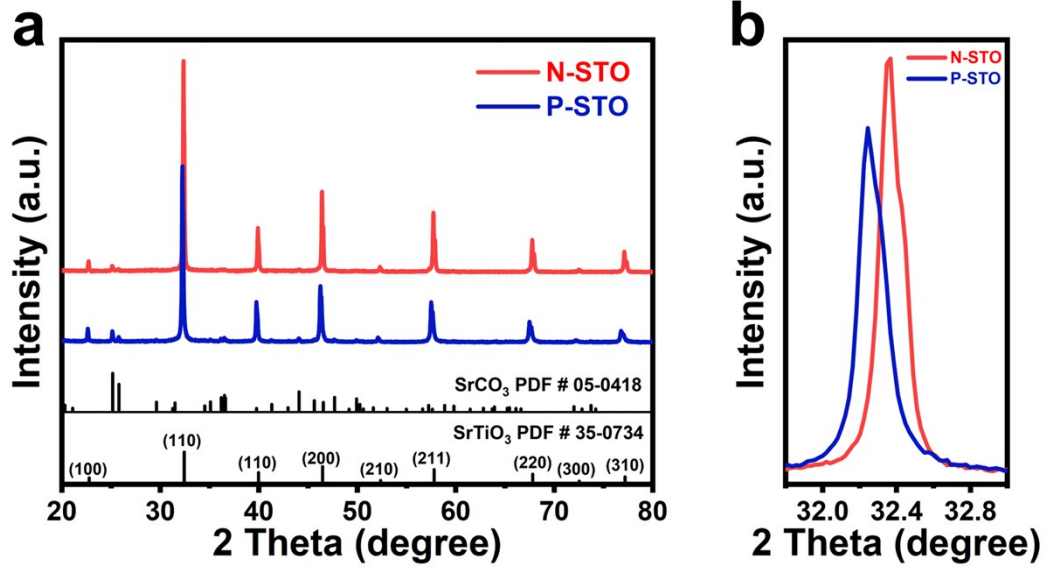
Fig. S9 (a) XRD patterns of N-STO and P-STO. (b) Comparison of their primary peak at 32.4°, demonstrating that the crystallinity of N-STO is higher than that of P-STO.
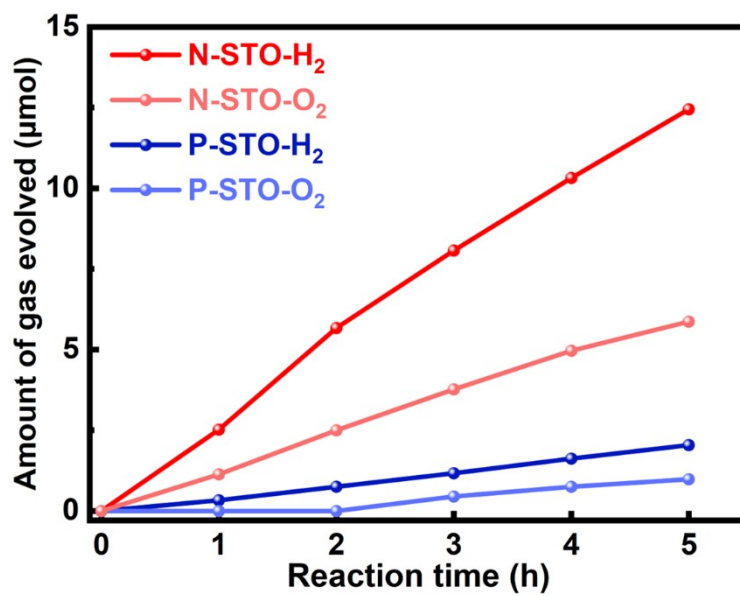
Fig. S10 Time courses of gas evolution during overall water splitting over N-STO and P-STO.
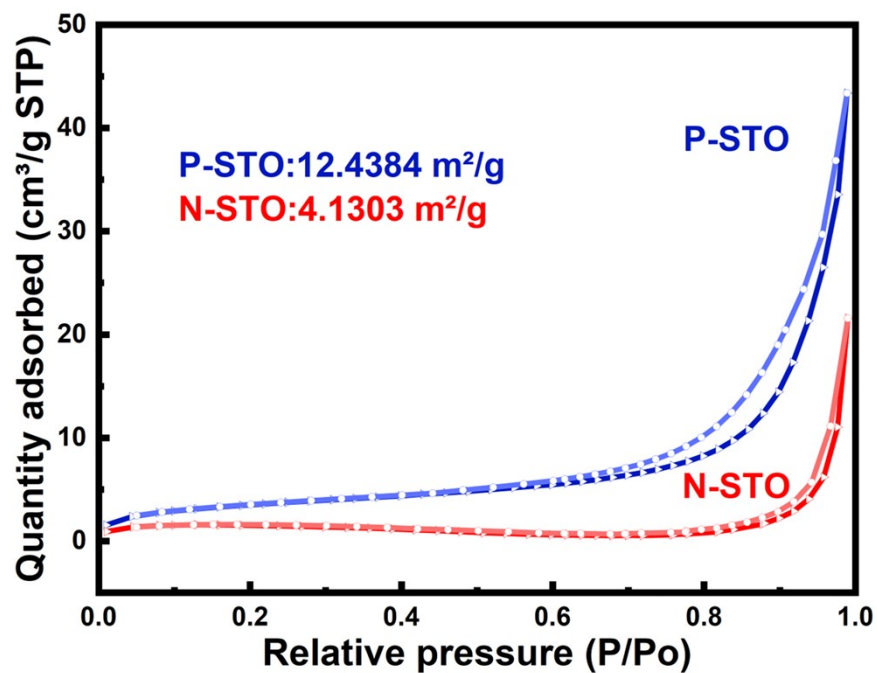
Fig. S11 Nitrogen adsorption-desorption isotherms of P-STO and N-STO. The test results show that the BET surface area of N-STO is 4.1303 m^2 g^{-1}, while the BET surface area of P-STO is 12.4384 m^2 g^{-1}. The BET surface area of P-STO is three times of that of N-STO, which was attributed to the existence of interconnected mesoporous structure inside P-STO.
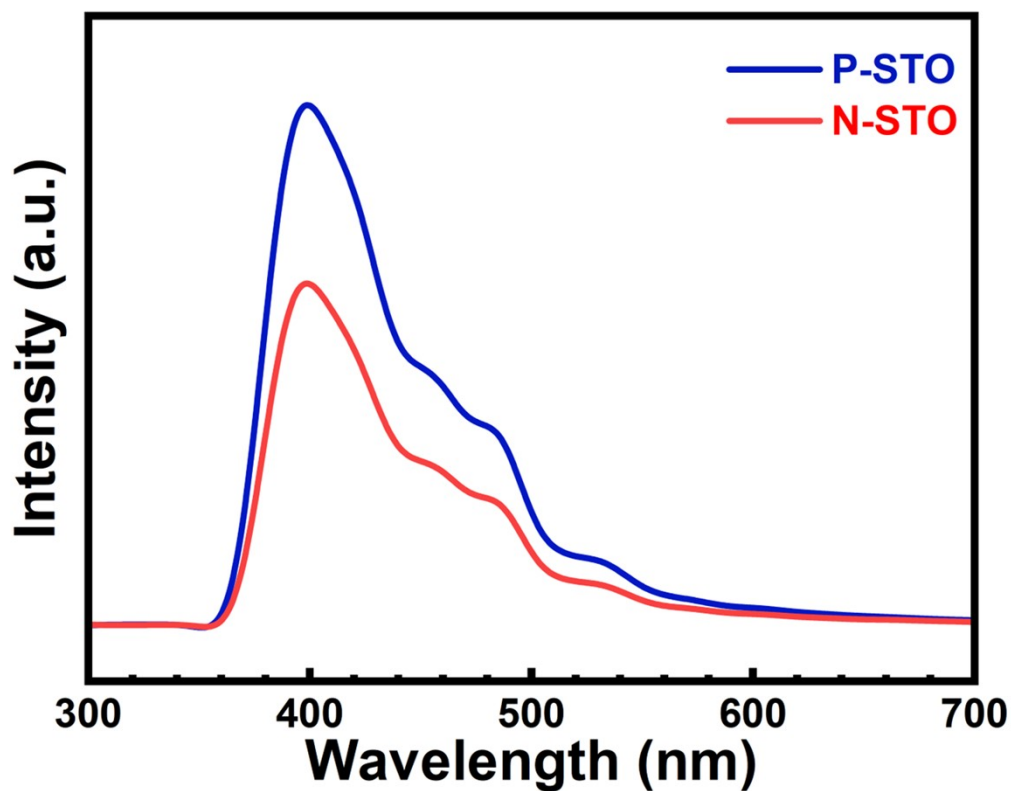
Fig. S12 PL spectra of N-STO and P-STO. The emission intensity of N-STO is lower than that of P-STO, indicating that the compounding rate of photoexcited electron-hole pairs in N-STO is lower. This lower intensity suggests that the nonradiative recombination of photogenerated electron-hole pairs in N-STO is reduced. A lower recombination implies that more electron-hole pairs are available to participate in photocatalytic reactions.
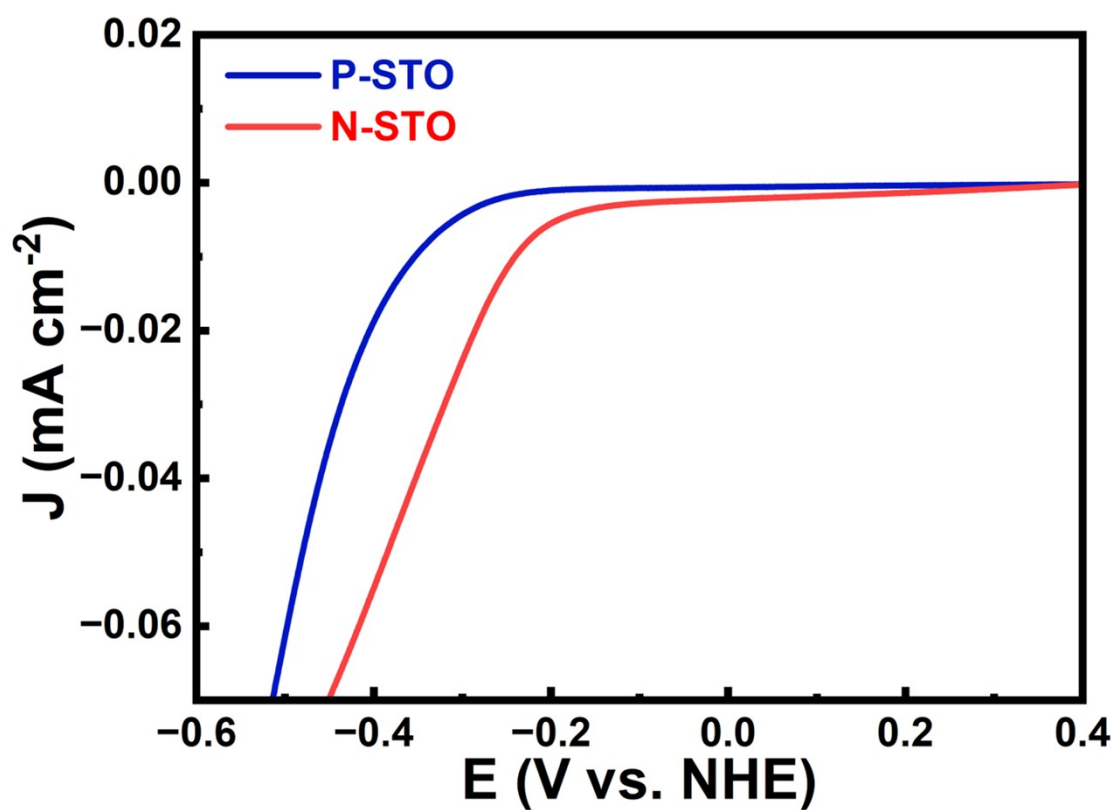
Fig. S13 LSV curves of N-STO and P-STO. N-STO possesses a lower overpotential than P-STO, indicating that N-STO has a higher energy conversion efficiency.
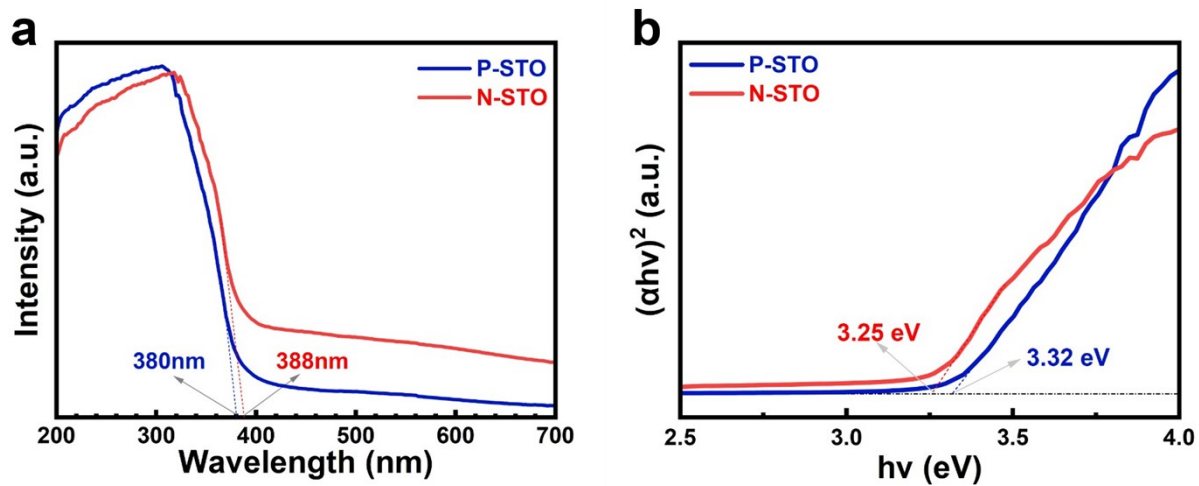
Fig. S14 (a) The UV-Vis diffuse reflectance spectra (UV-vis DRS) and (b) Kubelka-Munk function plots derived from the UV-vis DRS of N-STO and P-STO, showing that N-STO had a bandgap of 3.25 eV, while P-STO had a bandgap of 3.32 eV.
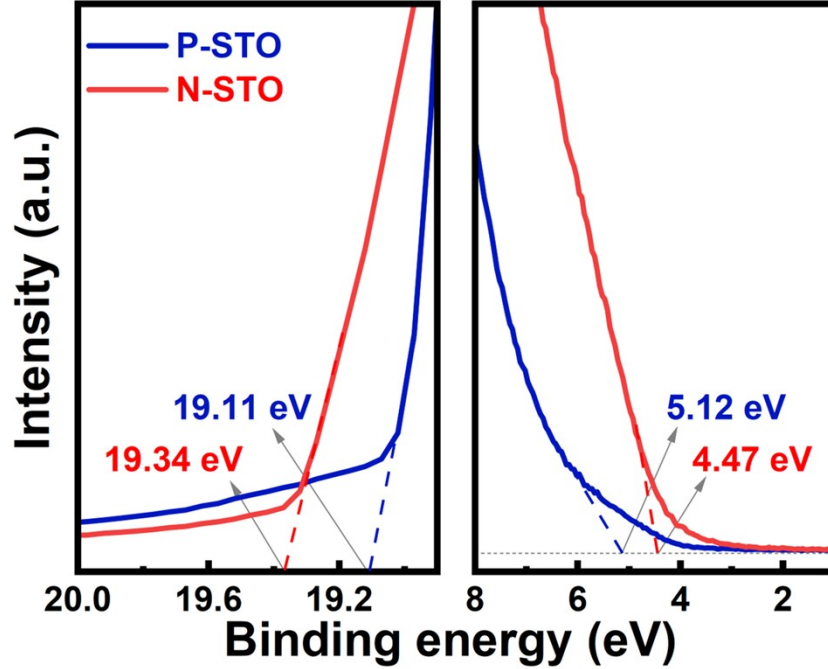
Fig. S15 UPS data for N-STO and P-STO. Helium Iα (hν = 21.22 eV) spectra of secondary electron cutoff (left panel) and UPS spectra in the valence band (VB) region (right panel) are shown. The intercept in the secondary electron cutoff (left panel) shows $E_{B,max}$ and right panel shows $E_{B,min}$, and the VBM was obtained by hν − ($E_{B,max}$ − $E_{B,min}$). The position of CBM with respect to VBM was defined by the optical band gap (3.32 and 3.25 eV).
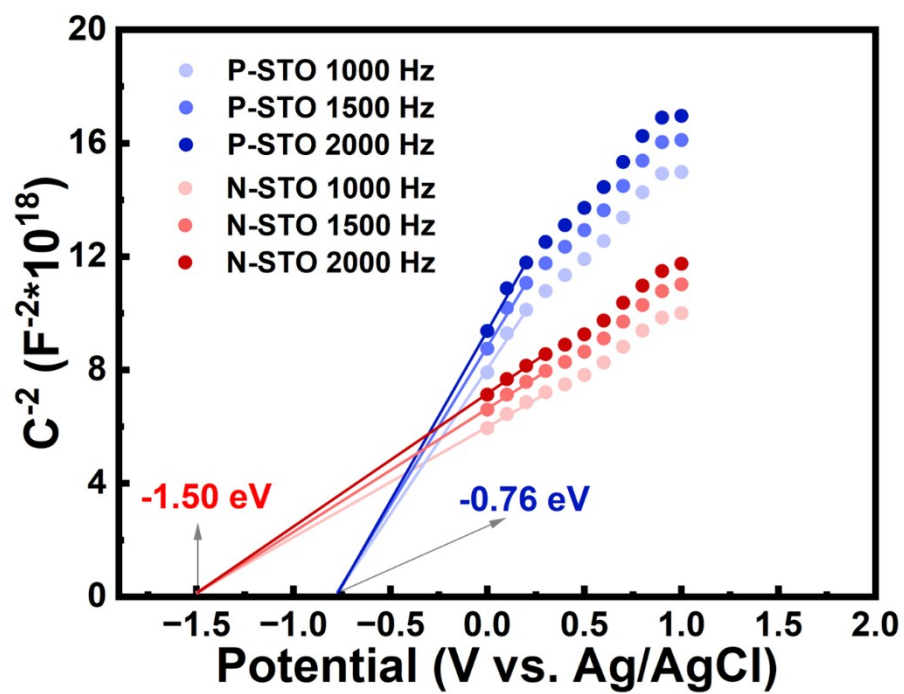
Fig. S16 Mott-Schottky curves of N-STO and P-STO, and the results were in general agreement with the calculations of the UPS and Kubelka-Munk function plots.

Table S1 AQY calculation. Calculated AQY values of CoOOH/Rh/Cr$_2$O$_3$-modified P-STO and N-STO (Rh, Cr, Co loading amount on 50mg SrTiO$_3$, 0.4 wt%, 0.2 wt%, 0.2 wt%) for photocatalytic overall water splitting.

Wavelengths (λ, nm)	Light power (mW/cm^2)	Sample	H$_2$ evolved (μmol/h)	AQY (‰)
280	3.76	N-STO	0.3	0.96711
		P-STO	0.09	0.29013
313	2.28	N-STO	0.24	1.14139
		P-STO	0.06	0.28535
334	2.86	N-STO	0.63	2.23836
		P-STO	0.18	0.63953
350	6.08	N-STO	1.23	1.96172
		P-STO	0.42	0.66985
360	5.82	N-STO	1.47	2.38119
		P-STO	0.45	0.72894
370	6.38	N-STO	0.9	1.29397
		P-STO	0.27	0.38819

Table S2. The relative area of each peak after the XPS pattern of Ti was subdivided into Ti^{4+} $2p_{3/2}$, Ti^{4+} $2p_{1/2}$, Ti^{3+} $2p_{3/2}$ and Ti^{3+} $2p_{1/2}$.

Sample	Ti^{4+} $2p_{3/2}$	Ti^{4+} $2p_{1/2}$	Ti^{3+} $2p_{3/2}$	Ti^{3+} $2p_{1/2}$
N-STO	67929.76	27037.72	48696.73	15571.45
P-STO	45942.31	19359.8	46161.58	12429.26

SrTiO$_3$ contains oxygen vacancies due to the dissociation of the Ti-O bond, where a small amount of lattice oxygen is released into the gas phase, which results in the creation of oxygen vacancies along with the release of free electrons from the lattice as shown in Equation (1). Then, the free electrons reduce Ti^{4+} to Ti^{3+} as shown in Equation (2), then the corresponding defect species are Ti^{3+} and oxygen vacancies[1]. The formation of one oxygen vacancy is accompanied by the formation of two Ti^{3+}. Therefore, we can calculate the percentage of oxygen vacancies based on the defect concentration of Ti^{3+}.

$$SrTiO_3 = SrTiO_{3-x} + \frac{1}{2}xO_2 + 2xe^- + xOv \qquad (1)$$

$$SrTiO_3 = SrTi(IV)_{1-2x}Ti(III)_{2x}O_{3-x} + \frac{1}{2}xO_2 + xOv \qquad (2)$$
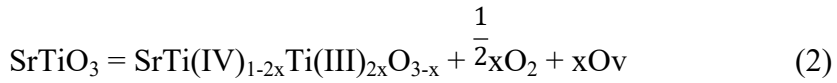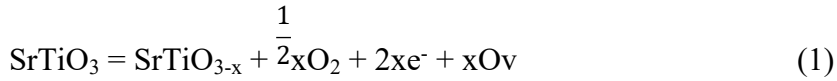
Table S3. Oxygen vacancy concentration calculated from Ti^{3+} and Ti^{4+}.

Sample	Oxygen vacancy concentration (%)
N-STO	6.72
P-STO	7.88

Table S4. The results of the fitted Nyquist plots for N-STO and P-STO.

Sample	R_s (Ω)	R_{ct} (Ω)
N-STO	3.37	16.76
P-STO	2.47	20.81

Notes: The charge transfer resistance (R_{ct}) typically signifies the impedance of electrochemical reactions at the semiconductor electrode surface, whereas the solution resistance (R_s) typically denotes the resistance to current flow within the electrolyte solution.

Reference

1. T. Takata and K. Domen, *J. Phys. Chem. C*, 2009, **113**, 19386-19388.